Energy Storage Materials 59 (2023) 102770

Contents lists available at ScienceDirect

Energy Storage Materials

journal homepage: www.elsevier.com/locate/ensm

High-entropy NaCl-type metal chalcogenides as K-ion storage materials: role of the cocktail effect

Che-Bin Chang [a], Ying-Rui Lu [b], Hsing-Yu Tuan [a,*]

[a] Department of Chemical Engineering, National Tsing Hua University, Hsinchu 30013, Taiwan
[b] National Synchrotron Radiation Research Center, 300 Hsinchu, Taiwan

ARTICLE INFO

Keywords:
Cocktail effect
High-entropy metal chalcogenides
Lithium-ion batteries
Potassium-ion batteries, shuttle effect

ABSTRACT

The drastic volume expansion of active materials and the shuttle effect of polychalcogenides hindered the development of anode materials for potassium-ion batteries (PIBs). Thus, various strategies have been used to overcome the negative effects associated with potassiation. Here, we propose a NaCl-type high-entropy metal chalcogenide (HEMC) prepared using a simple melting method as an anode material for PIBs. Unlike traditional high-entropy materials comprising inactive metals, NaCl-type HEMCs can realize the occupancy of cationic sites by active metals. We show that $AgSnSbSe_{1.5}Te_{1.5}$, a HEMC, produces short-range tiny cells during phase-change energy storage reactions, reconciling the participation of active and inactive metals to form various hetero-interfaces and different functional metal nanoparticles. The kinetic and density functional theory analysis showed that the formation of heterointerfaces decreased the diffusion energy barrier of K^+ and the inactive metal silver provided appropriate adsorption energy, suppressing the latent shuttle effect. The results show enhanced electrochemical performance owing to the elemental composition of high-entropy materials and the formation of tunable heterointerfaces and functional nanoparticles in electrochemical reactions, offering a new concept for the design of PIB anode materials.

1. Introduction

Large-scale energy storage technologies mitigate the intermittency of renewable energy sources and regulate grid systems' safety, stability, and reliability while avoiding the environmental problems caused by fossil fuels [1–3]. Lithium-ion batteries (LIBs) dominate the commercial market owing to their high energy density, high power, and low self-discharge [4–6]. However, the increasing energy demand and unevenly distributed lithium sources (0.0017 wt%) lead to a shortage of Li in the market [7]. In contrast, K is abundant in the earth's crust (1.542 wt%), about 1000 times more abundant than Li, and is evenly distributed [8]. Furthermore, the standard redox potential of K^+/K is −2.93 V vs. the standard hydrogen electrode (SHE), which is approximately similar to that of Li^+/Li (−3.04 V vs. SHE), indicating that comparable high energy and power densities can be achieved [9,10]. Meanwhile, because Al is an inert material for PIBs, Al foil ($2042 per ton) can replace the traditionally used Cu foil ($7951 per ton) [11,12]. Therefore, PIBs are expected to be used in next-generation energy storage technologies.

Nevertheless, PIBs lack suitable anode materials because the large ionic radius of K^+ (0.138 nm vs. 0.076 nm for Li^+) causes huge mechanical stress and results in potential active materials (e.g., Si) not in favor of K^+ [13]. Graphite is one of the most common anode material used for PIBs, providing a specific capacity of 279 mAh g^{-1} (KC_8) [14–16]. However, the increasing energy demand necessitates the development of high-capacity active materials for next-generation PIBs [17,18]. Thus, alloying and conversion-type reactions facilitating multiple electron transfers with high energy storage have been considered for anode materials [19–21]. The repeated insertion/extraction of K^+ causes anode materials to face three to four times volume expansion (K_3Sb~400%) [22]. The huge volume expansion undoubtedly leads to the pulverization of the material, breaking the solid electrolyte interface (SEI). The repeated repair and breakage of the SEI eventually deactivate the material. Moreover, the large size of K^+ hinders its diffusion in a host, limiting the solubility of the K^+ intercalation compounds [23]. The conversion reaction mainly occurs in metal chalcogenides, benefiting from weak metal chalcogenide bonds, as K^+ readily undergoes redox reactions with chalcogenides [24–26]. However, polychalcogenides are soluble in the electrolyte. When polychalcogenide anions are saturated, they are likely to deposit on the anode surface, which is known as the

* Corresponding author.
E-mail address: hytuan@che.nthu.edu.tw (H.-Y. Tuan).

https://doi.org/10.1016/j.ensm.2023.102770
Received 6 January 2023; Received in revised form 9 March 2023; Accepted 8 April 2023
Available online 9 April 2023

shuttle effect [27]. Besides, the loss of active materials is attributed to the high activity of polychalcogenides via nucleophilic addition or substitution reactions with carbonate-based electrolytes to form thiocarbonates [28].

Various strategies have been used to mitigate the adverse effects of potassiation, such as the nanocrystalline and synergistic effects [29,30]. Ge et al. reported that a Sb nanocrystal confined in a carbon nanofiber takes advantage of the nanocrystalline effect to reduce the active material to the nanometer level. This not only provided increased contact areas and alleviated the volume expansion caused by the insertion of K^+ [31–34]. Moreover, Cao et al. proposed that a hierarchical MoS_2/Sb heterostructure in a graphene framework improved the electrochemical performance. Besides, synergistic effect may not generate by heterointerface but stable intermediates phase. For example, Xiong et al. reported that binary metal Bi-Sb alloy nanoparticle embedded in a porous carbon matrix as PIBs anode material [35,36]. The reaction mechanism through in-situ XRD technique show that Bi-Sb nanoparticle form the stable intermediates phase of K(Bi, Sb) and finally convert to K_3(Bi, Sb) which having better electrochemical performance comparing the Bi and Sb nanoparticles with intermediates phase of KBi and KSb [37]. This is difficult to achieve with a single material as the synergistic effect relies on the rational design of composite materials. However, combining these two strategies for the development of superior anode materials has not been demonstrated.

High-entropy materials have been studied in electrochemical energy storage as they exhibit properties beyond those of their constituent elements [38]. In disordered multicomponent systems, a large entropy configuration is considered to stabilize the crystal structure (i.e., entropy-driven stabilization), providing multiple options for multicomponent systems and the potential to tailor functional properties [39–41]. Moreover, the chemical energy storage behavior of high-entropy anode materials produces a unique energy storage mechanism due to the influence of entropy. For example, Sarkar et al. reported a transition-metal-based high-entropy oxide (HEO) as an anode material for LIBs, indicating that the lithiated HEO forms short-range tiny cells below the detection threshold of X-ray diffraction (XRD). Mg enhanced the stability of the HEO rock-salt structure by acting as an inactive barrier, improving the cycling performance [42]. In addition, Zhao et al. reported a high-entropy sulfide as an anode material of sodium-ion batteries, where inactive metal particles precipitated after sodiation. Inactive metals act as barriers that isolate active material nanoparticles, avoid agglomeration, and reduce particle size [43]. These studies have shown that high-entropy materials have unique reaction mechanisms during phase-change energy storage reactions, but they all have two phenomena in common: (1) formation of short-range tiny cells and (2) production of various conversion products. These results agree with the goals of nanosize and synergistic effects, suggesting a unified approach in the development of next-generation high-efficiency energy storage anode materials.

Herein, we propose a NaCl-type high-entropy metal chalcogenide (HEMC) anode material. Active and inactive elements were configured via tunable anion and cation sites. We observed the electrochemical performance of five rock-salt solid solutions with different entropy configurations and found that an increase in entropy promoted the electrochemical performance. Operando X-ray absorption spectroscopy (XAS) was used to investigate the valence changes of each element during the potassiation of the HEMC to clarify the reasons for such improvement. Furthermore, we found that short-range tiny cells construct numerous heterointerfaces in the full potassiation/depotassiation state. Meanwhile, the density functional theory (DFT) clarified that various heterointerface formations reduce the diffusion barrier of K^+ in the electrode and that the exsolution of the inactive Ag metal exhibits a strong adsorption energy for polyselenium and polytelluride, inhibiting the shuttle effect [44]. We believe that the numerous heterointerfaces coupled with the strong adsorption of Ag are responsible for the enhanced electrochemical performance of HEMCs, providing unique insights into the "cocktail effect" in high-entropy materials.

2. Results and discussion

2.1. Feasibility of NaCl-type rock-salt structure

The single-phase high-entropy NaCl-type rock-salt structure has compositional flexibility and can avoid the reliance of the industry on a single metal source. Therefore, the elemental composition of NaCl-type rock-salt structures is discussed. The rock-salt structure has adjustable anion and cation sites so that appropriate elements can be accommodated for various application requirements [45]. Here, the $MSe_{0.5}Te_{0.5}$ system (M = Ag, Bi, Co, Cu, Fe, Ge, Mn, Nb, Sb, and Sn) was selected to evaluate the possibility of using potential metal elements for PIB anodes (Fig. S1). Because the NaCl-type rock-salt structure has anion and cation sites (Fig. 1a), the entropy calculation must be separated as follows [46]:

$$S = -R\left[\left(\sum_{i=1}^{M} x_i \ln x_i\right) + \left(\sum_{j=1}^{N} x_j \ln x_j\right)\right] \quad (1)$$

where i is the cation site, j is the anion site, and R is the gas constant. The anion-site entropy of the $MSe_{0.5}Te_{0.5}$ system is 0.61R, and the cation site comprising more than three metal elements (1.09R) satisfies the minimum entropy required for high-entropy materials ($\Delta S \geq 1.61R$) [47]. Fig. 1b presents the redox suitability among 14 metal ions on a logarithmic basis (base 10). All the pair correlations were obtained from a previous report [48]. The positive values indicate a tendency to substitute, whereas the negative values indicate no substitution tendency. Late transition metals such as Fe^{2+}, Co^{2+}, and Mn^{2+} have a strong substitution tendency owing to the charge effect and similar ionic radii. Meanwhile, the nontransition metals Bi^{3+} and Sb^{3+} suggest that greater electron delocalization generates a strong substitution tendency [49]. These trends can be used to evaluate chemical compatibility between different candidates in the $MSe_{0.5}Te_{0.5}$ system. We calculated the energy difference between the metal M randomly distributed in the $MSe_{0.5}Te_{0.5}$ rock-salt structure and the competing phases using DFT to estimate the mixing temperature of the $MSe_{0.5}Te_{0.5}$ system (Table S1). A lower mixing temperature offers enhanced feasibility because less thermal energy is required to mix the metal ions. However, it is not the absolute temperature of synthesis and can only be regarded as a numerical difference in the feasibility of synthesis [50,51]. The mixing temperature distribution diagram of 10 metal elements in the $MSe_{0.5}Te_{0.5}$ rock-salt structure is shown in Fig. 1c. Metals with a low mixing temperature (Ag, Cu, Mn, and Sb) more likely produced a single-phase high-entropy rock-salt structure. Meanwhile, based on the Hume–Rothery rule, the bond length of metal cations and chalcogenides is related to the degree of crystal strain, where small strains are conducive to the stability of single-phase crystal structures [52]. The bond length compared with those in the International Center for Diffraction Data (ICDD) and bond valence model (BVM) is shown in Fig. 1d, and the calculation detail of the BVM model is listed in Table S2. Co^{2+} and Sb^{3+} ions showed large bond length variations, indicating that these ions are softer, benefiting from the reduced local stress and promoting the formation of single-phase high-entropy rock-salt structures [53,54]. Fig. 1e presents the structure optimization result of 10 metal ions in the rock-salt structure. Ag, Co, Cu, Fe, Mn, and Sn generally maintained the rock-salt structure, indicating that they are more suitable for the rock-salt structure without considering the competing phase. Based on the redox suitability, mixing temperature, and bond length of metal ions in this high-entropy system, we selected the inactive metal Ag, which provides a strong adsorption energy for inhibiting the potential shuttle effect caused by polychalcogenides. Furthermore, Sb, Sn, Se, and Te act as active materials and ensure the generation of various heterointerfaces, utilizing the advantage of the high-entropy configuration.

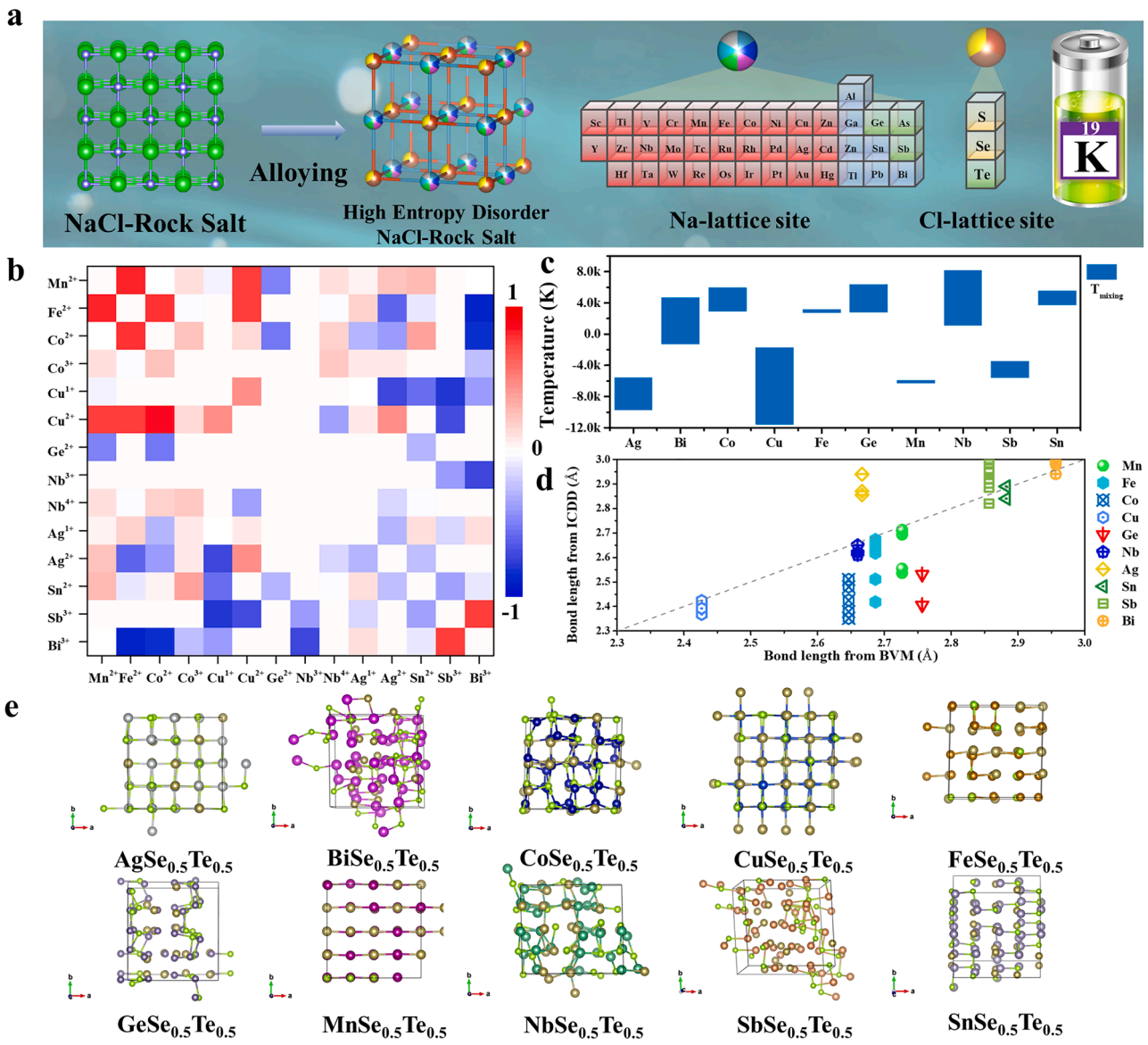

Fig. 1. Compatibility of the $MSe_{0.5}Te_{0.5}$ structure. (a) Schematic illustration of the high-entropy disorder NaCl-rock-salt structure. (b) Pair correlation for each ion couple with logarithm (10 base). (c) Distribution of the mixing temperature for each metal cation. (d) Comparison of the bond length from the ICDD and BVM model. (e) $MSe_{0.5}Te_{0.5}$ structure with different metal cations after geometric optimization.

2.2. Structural characterization

Five rock-salt-type materials were prepared by sealing quartz tubes in an environment under 10^{-3} torr with melting-state reactions at 1173 K. With the increase in metal cation amounts, the amounts of Se and Te also increase owing to the charge compensation mechanism, which balances the positive charge added due to the metal cation, thus enhancing the feasibility of the high-entropy system (Fig. 2a). The powder XRD pattern of each material is shown in Fig. S2. The observed XRD pattern showed only the low entropy metal chalcogenide (LEMC) with an orthorhombic structure (space group *Pnma*, JCPDS 48–1224). With the increase in entropy, all the other four materials showed a rock-salt cubic structure (space group $Fm\bar{3}m$, JCPDS 65–6604) without any impurities. Notably, the (200) facet of the cubic rock-salt structure slightly shifted toward a smaller angle, indicating that larger-atom alloys induced lattice expansion. The corresponding Rietveld refinements of the XRD patterns are shown in Fig. 2b and Figs. S3–S6, and the HEMC showed the lattice parameters of $Fm\bar{3}m$ [$a = b = c = 5.9959$ Å]. X-ray photoelectron spectroscopy (XPS) was used to confirm the valence states of the elements in the HEMC. The full survey is shown in Fig. S7; the fine scan of each element is shown in Fig. 2c. Two strong peaks of 374.0 eV ($Ag3d_{3/2}$) and 368.0 eV ($Ag3d_{5/2}$) were observed in the Ag 3d spectrum. The binding energy comprised Ag_2Se ($Ag3d_{3/2}$, 373.9 eV; $Ag3d_{5/2}$, 368.1 eV) [55]. In the Sn 3d spectrum, two doublet peaks at 494.9 eV (Sn $3d_{3/2}$) and 486.5 eV (Sn $3d_{5/2}$) indicating $Sn^{4+}$and slight surface oxidation, respectively, were obtained [56]. In the Sb 3d spectrum, 539.6 eV (Sb $3d_{3/2}$) and 530.3 eV (Sb $3d_{5/2}$) belonged to Sb^{3+}, accompanied by O 1 s surface oxidation at 532.7 eV. Meanwhile, the Se 3d spectrum was divided into two subpeaks at 54.4 eV (Se $3d_{5/2}$) and 53.5 eV (Se $3d_{3/2}$), which belonged to Se^{2-} and Te $3d_{3/2}$. Te $3d_{5/2}$ can be assigned to the peak at 586.6 eV, whereas the 576.2-eV peak belongs to Te^{4-}; the 582.7 eV (Te $3d_{3/2}$) and 572.3 eV (Te $3d_{5/2}$) peaks were assigned to Te^{2-}, representing the bond between Te and metal cations. Graphite was added to the ball milling procedure to reduce the dimensions and protect the materials. After ball milling, the particle size of all materials was reduced to <5 μm (Fig. S8). The materials had similar sizes without phase transformation (Fig. S9), providing a unified standard for subsequent electrochemical measurements to discuss the

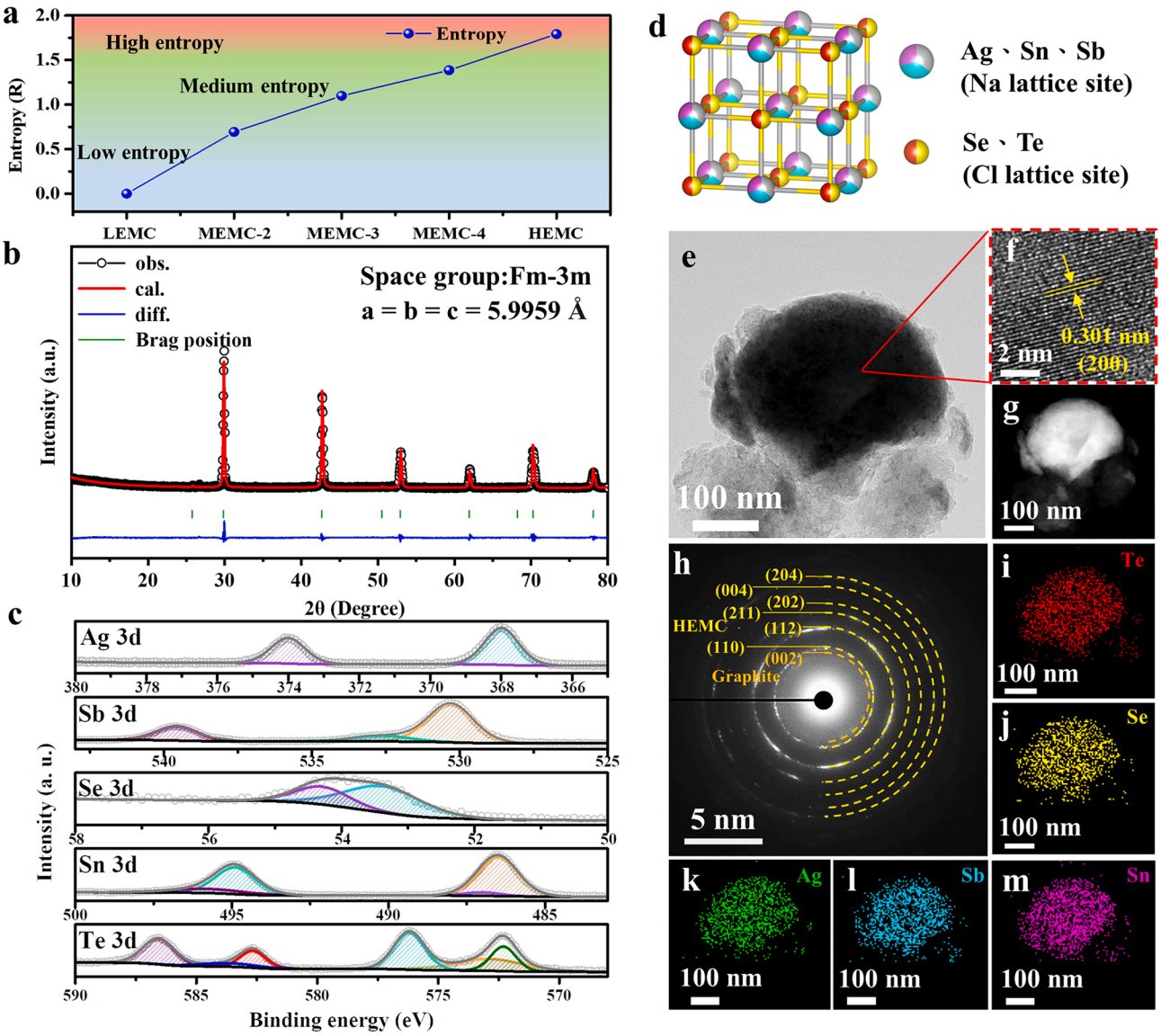

Fig. 2. Morphology and structure characterization. (a) Configuration entropy depending on the number of cations. (b) Rietveld refinement plot of HEMC. (c) High-resolution XPS survey of Ag, Sn, Sb, Se, and Te, respectively. (d) Crystal structure of NaCl-type HEMC. (e) TEM image, (f) HRTEM image, (g) HAADF image, and (h) SAED pattern and the corresponding EDS elemental mapping of HEMC@C.

influence of entropy. As examined using thermogravimetric analysis, the carbon content was identified as 33.1% (Fig. S10). The Raman spectra of HEMC and HEMC@C were collected (Fig. S11). With graphite addition, two peaks were detected at approximately 1343 and 1584 cm^{-1} corresponding to the D and G bands, respectively [57]. The Brunauer–Emmett–Teller surface area of HEMC@C was evaluated using nitrogen adsorption/desorption isotherms (Fig. S12). The HEMC@C had a surface area of 176.4 $m^2 g^{-1}$; a typical nonporous isotherm curve was obtained [58]. The local fine structure of HEMC@C was confirmed using TEM, as shown in Fig. 2c, and a few layers of graphene were attached to the HEMC (Fig. S13). A (200) facet belonging to the rock-salt structure can be observed from the high-resolution TEM (HRTEM) image (Fig. 2d), whereas HEMC particles encapsulated with graphite can be observed from the high-angle annular dark field (HAADF) image (Fig. 2e). The D-spacing of the HEMC from the selected area electron diffraction (SAED) pattern (Fig. 2f) corresponds to the Rietveld refinement result shown in Fig. 2b. Figs. 2g–k show the energy-dispersive X-ray spectroscopy (EDS) element mapping images. Ag, Sn, Sb, Se, and Te were evenly distributed in the HEMC particles. Further, scanning electron microscopy coupled with EDS showed the stoichiometric element ratios (Fig. S14).

2.3. Electrochemical performance

The electrochemical performance of different entropy configurations was evaluated in a CR-2032 coin cell using 1 M KFSI in DMC as the electrolyte and hand-made K foil as the counter electrode. Figs. 3a–e show the initial three-cycle cyclic voltammetry (CV) curves with different entropy configurations. The scan rate and working window were 0.01 mV s^{-1} and 0.01–3.00 V (vs. K^+/K), respectively. All the entropy configuration materials showed a significantly larger scanning area in the first cycle than those in the subsequent cycles, which was caused by the irreversible side reaction and the formation of the SEI layer on the surface of the material [59]. In the second and third CV curves, the higher coincidence represents the better reversibility of the material. For quantifying the coincidence, we define the area difference (A_{dif}) as

$$A_{dif} = \frac{|A_{3rd} - A_{2nd}|}{A_{2nd}} \times 100\% \quad (2)$$

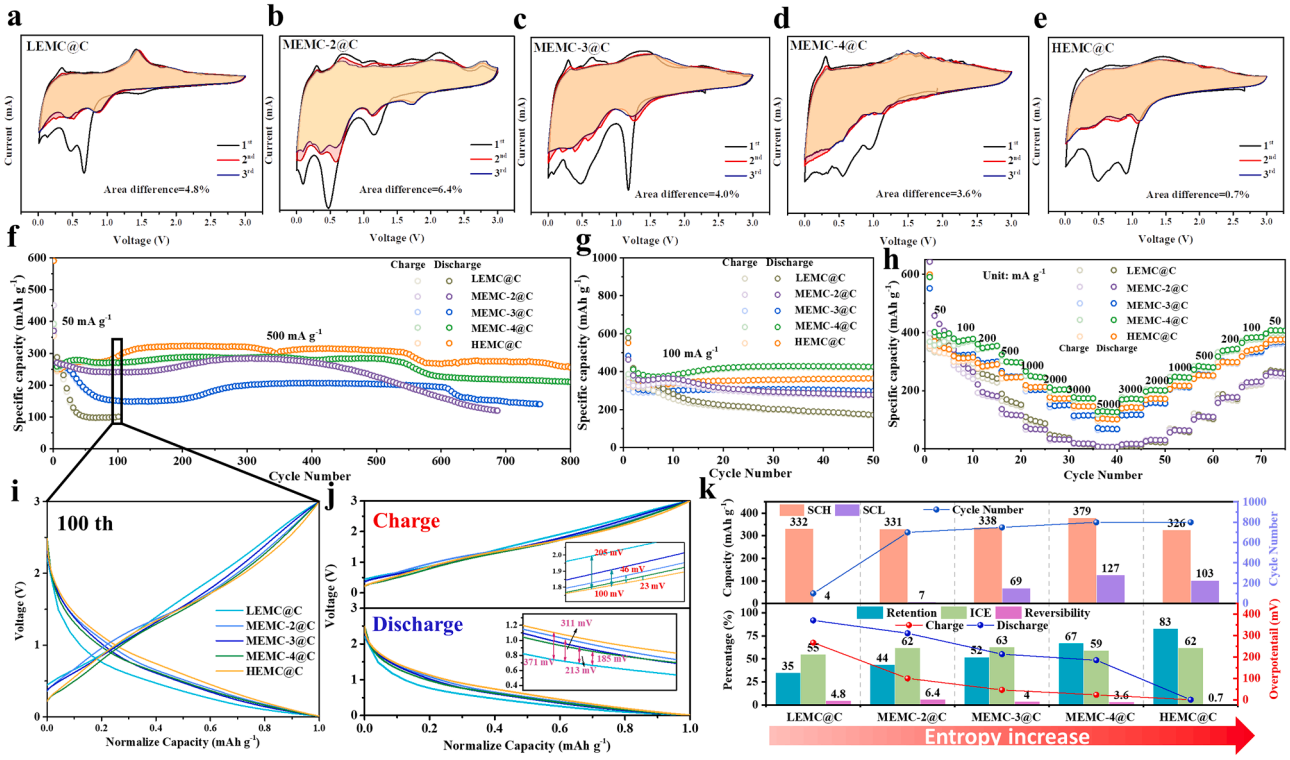

Fig. 3. Electrochemical performance of different entropy electrodes. First three-cycle CV profiles and corresponding area differences of (a) LEMC@C, (b) MEMC-2@C, (c) MEMC-3@C, (d) MEMC-4@C, and (e) HEMC@C. (f) Cycling stabilities, (g) cycling performances, and (h) rate capabilities of LEMC@C, MEMC-2@C, MEMC-3@C, MEMC-4@C, and HEMC@C. (i) Normalized QV profile and (j) overpotential analysis of different entropy electrodes. (k) Comparison of specific capacity at high and low current densities (SCH and SCL), cycle number, retention, ICE, CV area difference, and overpotential of different entropy electrodes.

A_{2nd} and A_{3rd} correspond to the area of the second and third cycles, respectively. This area difference represents the deviation ratio between the scanning area of the third cycle and the area of the second cycle, which can be used as a qualitative measure of reversibility. According to the calculated results, the A_{dif} values of LEMC@C, MEMC-2@C, MEMC-3@C, MEMC-4@C, and HEMC@C were 4.8%, 6.4%, 4.0%, 3.6%, and 0.7%, respectively. The A_{dif} had an increasing tendency with a higher entropy configuration. In other words, the increase in entropy configuration had an impact on the cycle stability of the battery. According to the reaction mechanism (discussed in detail later), various heterointerfaces were composed of short-range tiny cell formations, boosting the redox reaction. The cycling performance (Fig. 3f) of the LEMC@C began to show a downward trend after 80 cycles, and MEMC-2@C and MEMC-3@C showed a capacity decline at 400 and 600 cycles, respectively. Notably, the HEMC@C and MEMC-3@C exhibited satisfactory stability and maintained a relatively stable capacity for 800 cycles. The specific capacity fluctuated upon increasing the cycle number, which can be explained as follows. First, the materials were prepared by the melting method, and low-energy ball milling (200 rpm) was conducted with graphite. The particle size was larger than 200 nm, which led to the uneven potassiation rate of these particles. This phenomenon slightly increased the specific capacity before 100 cycles. Notably, the rising amplitude of the specific capacity is due to the entropy increase because an increased number of tiny cells and heterointerfaces was formed as the entropy increased. Second, after 100 cycles, the electrochemical performance of different anode materials became steady owing to the construction of tiny cells and heterointerfaces, demonstrating the advantages of the nanocrystalline and synergistic effects. Finally, after 500 cycles, the specific capacity gradually decreased as the graphite was coated by low-energy condition and provided basal protection only, leading to partial active material deactivation. The cycling performance of different entropy electrode without carbon coating was shown is Fig. S15, the capacity fading rapidly because the larger particles size and lack protection. The current density cycling performances of electrodes are shown in Fig. 3g. At a low current density of 100 mA g^{-1}, LEMC@C, MEMC-2@C, MEMC-3@C, MEMC-4@C, and HEMC@C had reversible specific capacity of 224, 313, 306, 419, and 351 mAh g^{-1}, respectively. Take advantage of multielectron transfer, all anode materials except the LEMC@C exhibited higher specific capacity than graphite anode materials. Further, Fig. 3h compares the rate capability of each entropy configuration electrode. At a high current density of 5000 Ma g^{-1}, LEMC@C, MEMC-2@C, MEMC-3@C, MEMC-4@C, and HEMC@C provided reversible capacity of 4, 7, 69, 127, and 103 mA g^{-1}, respectively, revealing that MEMC-4@C and HEMC@C exhibited significantly improved rate performances compared with the other electrodes. Moreover, when the current density gradually returned from 5000 to 50 mA g^{-1}, MEMC-3@C, MEMC-4@C, and HEMC@C returned to the specific capacity of the initial current density of 50 mA g^{-1}, whereas LEMC@C and MEMC-2@C did not maintain the original specific capacity at a low current density. These results indicate that K^+ has fast and stable redox kinetics in electrodes with high-entropy configuration. Fig. 3i shows the QV curves of electrodes with various entropy configurations after 100 cycles, which can accurately reflect the total resistance of redox reactions. However, the different specific capacity led to the distortion of the comparison. Hence, the specific capacity was normalized and divided into charging/discharging parts, as shown in Fig. 3j. Moreover, Se was the intersection of the five entropy configuration materials; thus, we used the redox potential of Se (approximately 1.78 and 0.95 V for the cathodic and anodic reactions, respectively) as a benchmark to clarify the influence of entropy configuration on the overpotential. The upper part of Fig. 3j shows that the HEMC@C had the smallest Se reduction overpotential, whereas the overpotentials of LEMC@C, MEMC-2@C, MEMC-3@C, and MEMC-4@C increased by 267, 100, 46, and 23 mV, respectively. The lower part of Fig. 3j also shows that the HEMC@C had the highest oxidation overpotential, whereas those of LEMC@C, MEMC-2@C, MEMC-3@C, and MEMC-4@C

were reduced by 371, 311, 213, and 185 Mv, respectively. These results show that the high-entropy configuration contributes to the reduction of the overpotential through the gradual increase in the entropy configuration, increasing heterointerfaces. The synergistic effect between multicomponent heterogeneous interfaces contributes to the stable redox reaction of anions and cations [60]. Electrode surfaces after the 50th and 100th cycles are shown in Fig. S16. At the 50th cycle, LEMC@C, MEMC-2@C, and MEMC-3@C showed noticeable cracks, whereas MEMC-4@C and HEMC@C maintained intact electrode surfaces. When the cycle number was increased to 100, the cracks in LEMC@C, MEMC-2@C, and MEMC-3@C became large and even propagated to the current collector. In the meantime, MEMC-4@C and HEMC@C maintained crack-free surfaces. Fig. 3k shows the performance comparisons of electrodes with various entropy configurations, where the relationship between the performance indicators and entropy is revealed. The capacity retention, reversibility, cycle number, specific capacity at high rates (SCH), and overpotential demonstrated positive correlations with the increase in the entropy configuration. In contrast, the low-rate performance (SCL) and the initial Coulombic efficiency (ICE) were not relevant to the entropy configuration. The low-rate performance occurred because the theoretical capacity of the five entropy configurations did not remarkably differ (Table S3). The capacity contribution of graphite can be neglected since there is nearly no capacity at a high current density (Fig. S17). The ICE mainly represented an irreversible oxidation reaction on the surface of the material and the formation of the SEI layer. Therefore, for the full-cell system, which did not have a sufficient K^+source, the ICE became a critical issue for high-energy-density full cells [61]. All entropy materials had an appropriate ICE of around 60% except the LEMC@C, providing great potential in full-cell systems.

CV measurements were performed at different scan rates ranging from 0.1 to 0.9 mV s^{-1} to further understand how the increase in entropy composition affects the electrochemical performance of the electrode. The peak current (i) and the scan rate (v) of the power law formula were

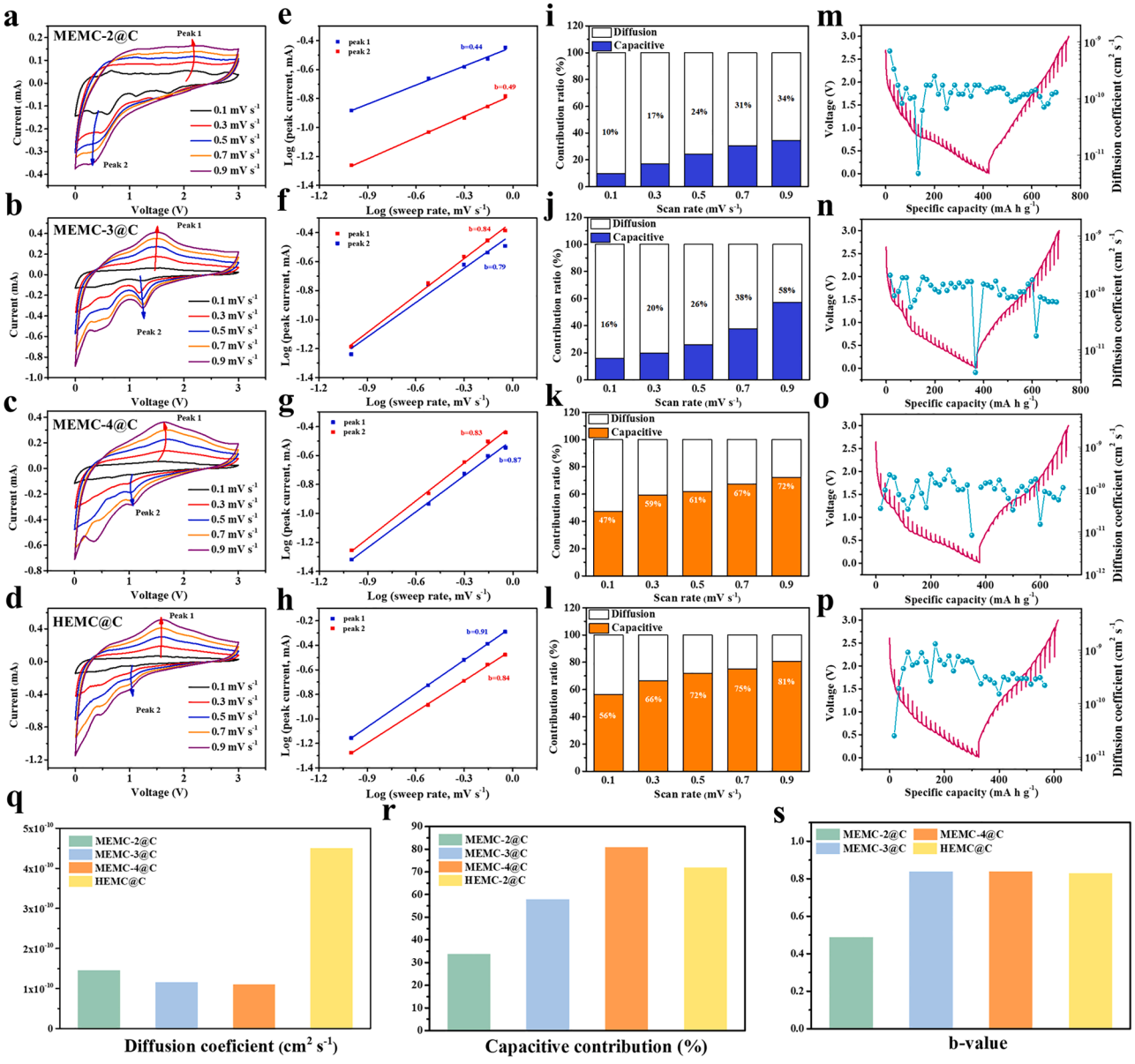

Fig. 4. Kinetic analysis of different entropy electrodes. (a–d) CV profiles at different scan rates of MEMC-2@C, MEMC-3@C, MEMC-4@C, and HEMC@C. (e–h) Linear correlation between the logarithmic peak current and sweep rate, (i–l) capacitive contribution, and (m–p) diffusion coefficient with the corresponding QV curves of different entropy electrodes. Summary of (q) average diffusion coefficient and (r) capacitive contribution at a scan rate of 0.9 mV s^{-1} and b value of different entropy electrodes.

used to calculate the reaction behavior (Eq. (3)) [62]:

$$i = av^b \tag{3}$$

when I is linearly related to v, that is, $b = 1$, it indicates that the electrochemical reaction is dominated by the surface control mechanism. When i is related to the square root of v ($b = 0.5$), the reaction is controlled by diffusion. For a typical electric double-layer capacitor (EDLC), no redox reaction occurs, and only the adsorption reaction takes place [63]. This material type usually has a huge specific surface area. Compared with that synthesized using the melting method, the HEMC exhibits relatively large particle size without pores, resulting in a small specific surface area. Moreover, because of the formation of the SEI film, the adsorption activity of the EDLC is reduced, demonstrating that the contribution of the EDLC can be excluded, and the measured linear relationship is caused by surface heteroatom moieties [64]. Figs. 4a–d show the CV curves of MEMC-2@C, MEMC-3@C, MEMC-4@C, and HEMC@C at different scan rates. As the scan rate increased, a gradually increasing response current was observed. Notably, the response current of LEMC@C did not increase as the scan rate increased, indicating poor cycle stability (Fig. S18). According to the fitting results, the b values of the anode and cathode current peaks of MEMC-2@C, MEMC-3@C, MEMC-4@C, and HEMC@C (Figs. 4e–h) were 0.44, 0.79, 0.91, and 0.87 (anodic), and 0.49, 0.84, 0.84, and 0.83, respectively (cathodic), illustrating that the HEMC@C was mainly under surface control. The specific pseudocapacitance contribution at different scan rates can be further obtained using Eq. (4) [65]:

$$i = k_1 v + k_2 v^{\frac{1}{2}} \tag{4}$$

In the above equation, $k_1 v$ and $k_2 v^{\frac{1}{2}}$ represent the control of pseudocapacitance and diffusion behavior, respectively. By calculating the value of k_1, the contribution value of pseudocapacitance and diffusion behavior control can be quantified. Figs. 4i–l show the capacitive contribution increases of different entropy configuration electrodes with sweep rates from 0.1 to 0.9 mV s^{-1}. The capacitive contribution values of MEMC-2@C, MEMC-3@C, MEMC-4@C, and HEMC@C were 34%, 58%, 81%, and 72%, indicating that the capacitive contribution does not absolutely increase with the growth of entropy configuration, but it more likely increases with the composition of surface heteroatoms. The QV curves and the corresponding diffusion coefficients are plotted in Figs. 4m–p. Using the galvanostatic intermittent titration technique (GITT), the potassium-ion diffusion coefficient D_{K^+} can be calculated based on Fick's second law using Eq. (5):

$$D_{K^+} = \frac{4}{\pi\tau}\left(\frac{m_b V_M}{M_b S}\right)^2 \left(\frac{\Delta E_s}{\Delta E_\tau}\right)^2 \tag{5}$$

where m_b, V_M, M_b, S, and τ represent the active material mass, molar volume, molar mass, surface area, and relaxation time of the electrode, respectively. ΔE_s is the voltage difference between the steady states, whereas ΔE_τ is the voltage difference during the pulse process (Fig. S19). Based on Eq. (5), D_{K^+} corresponding to various entropy configurations ranged from 10^{-9} to 10^{-11} cm^2 s^{-1}. Notably, HEMC@C had about four to five times higher D_{K^+} than the other entropy configurations. This possibly benefited from the formation of numerous heterointerfaces, which reduced the diffusion barrier of K^+ and effectively promoted the alloying and conversion reactions of K^+. Fig. 4q integrates the b value, capacitive contribution, and D_{K^+} of each entropy configuration electrode. Notably, the D_{K^+}, b value, and capacitive contribution did not absolutely increase with the growth of the entropy configuration. This behavior illustrated that the elemental composition is a key factor that affects the dynamics of K^+ because different heterointerfaces influence the electrochemical performance differently.

2.4. Mechanism derivation

Operando XAS was introduced to detect the average valence state of each element in the HEMC@C to infer the reaction mechanism (Fig. 5a). The K edge absorption spectra of Ag, Sn, Sb, Se, and Te were measured in fluorescence mode at a current density of 100 mA g^{-1}, as shown in Figs. 5b–f. The selected open circuit potentials (OCPs) (0.01 and 3.00 V) of the XAS spectra are plotted in Figs. 5g–k, and waterfall patterns are plotted in Fig. S20 to easily understand the energy change during potassiation/depotassiation. Herein, 60% of the edge jump height was used as the indicator of the valence state to evaluate the valence variations of HEMC@C during the potassiation/depotassiation process. The energy shift of the X-ray absorption near-edge structures (XANES) was obtained as follows:

$$\Delta E = E(0.6) - E_0(0.6) \tag{6}$$

Fig. 5b shows the Te K edge XANES spectrum of the first cycle. The initial absorption peak was at 31,814.8 eV. As the degree of potassiation deepens, the Te K edge gradually moved to higher energy, and the white line moved downward until the end of discharge (EOD). The edge energy was located at 31,816.0 eV (+1.2 eV), indicating that the formation of the K–Te intermediate phase involved K_2Te, K_2Te_3, and K_5Te_3. Moreover, the decrease in the white line can be attributed to the screening effect between K and Te. During depotassiation, the Te K edge gradually moved to low energy, and the white line gradually increased until the end of the charging process. The edge energy was 31,814.5 eV (−1.5 eV), which was close to the edge energy of the OCP state, possibly due to the recombination with metal cations. Fig. 5c shows the Ag K edge XANES spectrum collected in the first cycle. The K edge absorption energy of Ag under the OCP was 25,515.9 eV. Upon potassiation, the K edge absorption energy of Ag gradually shifted toward high energy, and the white line increased. At the EOD position, the edge energy was 25,516.6 eV (+0.7 eV). The similar energy and oscillation tendency with those of the metal Ag indicate that Ag is an inactive metal, consistent with a previous report [66]. Upon further performance of the charging process, the Ag K edge absorption energy shifted toward the initial state (25,515.9 eV (−0.7 eV)), and the white line gradually decreased, indicating recombination with anions. The in situ EIS of HEMC@C also supported the result of Ag exsolution and recombination (Fig. S21). Fig. 5d shows the Sn K edge XANES spectrum. The initial edge energy was 29,198.6 eV. Upon potassiation, the Sn K edge moved to higher energy with decreased white line, and the edge energy of the EOD state was 29,199.3 eV (+0.7 eV). In theory, as K^+ is more electropositive than Sn, lower edge energy must be obtained during Sn potassiation. However, the results showed that Sn moved to higher energy, as shown in the XANES results of LIBs [67]. It is considered that an alloy reaction between two different metals with dissimilar natures promotes charge transfer and superimposes a new covalent bond on the metal bond between Sn and K. Thus, delocalized electrons can freely slide between each other to minimize electrostatic energy [68]. In addition, the shift of the white line was not the same as that of Ag, indicating that charge transfer occurred between Sn and K, resulting in the reduction of 5p holes for Sn [69]. The above results support the production of KSn in complete potassiation. During the charging process, the Sn K edge still shifted to high energy, and the final edge energy was 29,200.5 eV (+1.2 eV), consisting of the metallic state of Sn (29,200.4 eV). The product after depotassiation is inferred to be metal Sn. Fig. 5e shows the XANES spectrum of the Se K edge. The initial edge energy at the OCP was 12, 657.7 eV. The Se K edge moved to higher energy, and the white line gradually decreased during potassiation and finally achieved an edge energy of 12,658.5 eV (+0.8 eV), indicating the formation of potassium polyselenide (K_2Se, K_2Se_3, K_2Se_5, and K_2Se_2) [70]. During depotassiation, the Se K edge moved to lower energy, and the final edge energy was 12,657.8 eV (−0.7 eV), which was close to the initial edge energy, similar to the condition of Te. However, the white line continued to decrease, representing the holes in the Se 4p decrease, which may

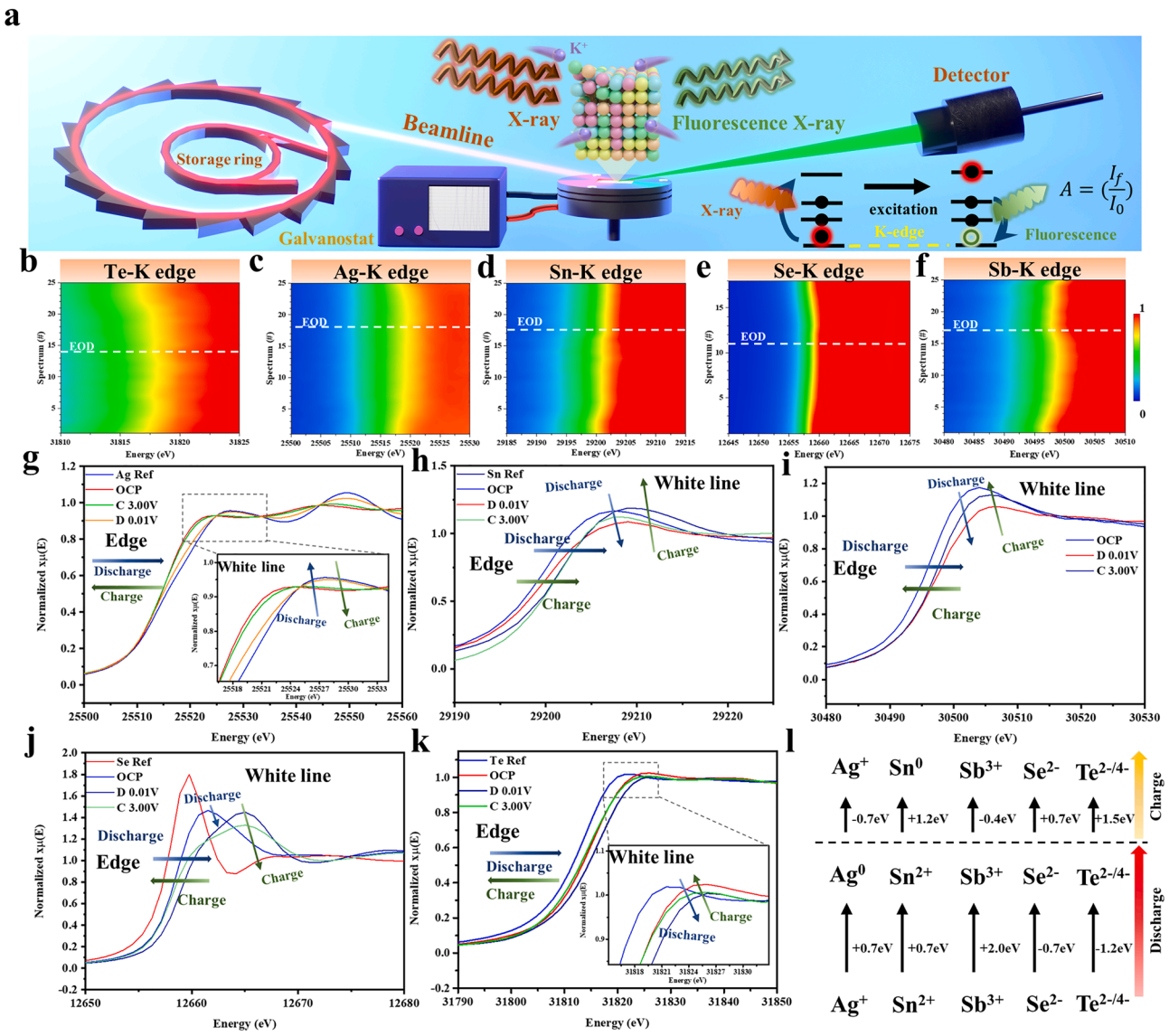

Fig. 5. Operando fluorescence XAS. (a) Schematic illustration of the electrochemical setup of operando fluorescence XAS. Evolution of operando (b) Te-K edge, (c) Ag-K edge, (d) Sn-K edge, (e) Se-K edge, and (f) Sb-K edge XANES in the HEMC@C electrode. Normalized XAS spectra at selected potentials of OCP (3.00 and 0.01 V) performed at the (g) Ag-K edge, (h) Sn-K edge, (i) Sb-K edge, (j) Se-K edge, and (k) Te-K edge. (l) Transformation of valence state and edge energy of each element in HEMC@C.

have been caused by the influence of the heterogeneous interface between Se and Te. Fig. 5f shows the Sb K edge XANES spectrum. The initial edge energy was 30,495.0 eV. During potassiation, the Sb K edge moved toward higher energy, and the white line gradually decreased. The final edge energy was 30,497.0 eV (+2 eV). These results were similar to those obtained for Sn, indicating similar charge transfer behaviors. Notably, the edge energy changed more than that of Sn because of the greater charge transfer (KSn, $1e^-$; K_3Sb, $3e^-$). During the charging process, the Sb K edge moved to a lower energy of 30,496.6 eV (−0.4 eV), implying the deinsertion of K^+. Fig. S22 shows the ex situ XPS spectrum of HEMC@C with various potentials. The Ag 3d ex situ XPS spectrum of HEMC@C is shown in Fig. S22a. The characteristic peaks of 374.6 and 368.6 eV were observed at the OCP corresponding to the characteristic peaks of the initial material of the HEMC@C. During the discharge process, an additional peak was observed at 377.3 eV, indicating K_{2s} characteristic peaks. Meanwhile, the peaks of Ag $3d_{5/2}$ and $3d_{3/2}$ shifted to 373.7 and 366.9 eV at 0.01 V, respectively, representing the exsolution of metallic silver. The characteristic peaks of Ag $3d_{5/2}$ and $3d_{3/2}$ shifted to higher binding energies at 374.3 and 368.3 eV, which were close to the initial characteristic peaks. Fig. S22b shows three peaks at 497.4, 495.8, and 487.3 eV corresponding to the oxidation peak of Sn and the characteristic peak of the HEMC@C. At the EOD, the three characteristic peaks at 493.0, 484.6, and 483.1 eV accompanied by oxidation peaks were observed because of the potassiation product formation [71]. When the voltage returned to 3.00 V, the two peaks were at 459.3 and 486.9 eV, representing the reduction of Sn. Fig. S22c shows that the two peaks of the HEMC@C shifted toward lower energy. The characteristic peak of Sb^0 was generated at 529.3 eV. The typical dealloying peaks of Sb and K at 531.4 eV corresponded to Sb^{3+} [72]. Fig. S22d shows two HEMC@C peaks, which shifted to lower energy during potassiation. Upon depotassiation, the peaks went back to high energy, revealing the conversion reaction between Se and K [73]. In Fig. S22e, the peaks at 576.8 and 573.4 Ev were observed under the OCP, contributed by the surface oxidized TeO_x and HEMC@C. At a potential of 1.00 V, the HEMC@C characteristic peak disappeared, and new peaks appeared at 571.9 and 570.3 eV, which corresponded to K_xTe ($0 < x \leq 2$) [74]. The characteristic peak at 569.5 eV was observed at 0.01 V, which corresponded to the generation of K_2Te. Further into the

depotassiation process, the characteristic peak of 570.7 eV was observed at 3.00 V, indicating that the product would not return to the initial HEMC@C structure after depotassiation. Fig. 5l summarizes the valence and edge energy shift during fully charge/discharge states, enabling the identification of the potassiation/depotassiation product. When the HEMC@C with a rock-salt structure reacts with K^+, the crystal lattice expands until it cannot withstand the expansion and then cracks into tiny unit cells and does not return to the original high-entropy rock-salt structure after depotassiation. The diffraction peaks were collected at a constant voltage, and a strong peak of HEMC@C was observed around 29.8° at OCP. As the voltage dropped to 1.00 V, the diffraction peak of HEMC@C shifted to a small angle, indicating that the crystal lattice expanded, caused by the insertion of K^+ into the cation sites of the rock-salt structure (Fig. S23). The subsequent potassiation process showed that the diffraction peak of HEMC@C gradually weakened, illustrating that the rock-salt structure could not withstand the lattice expansion and produced short-range tiny crystallites lower than the detection limit of the instrument [75]. To confirm the formation of heterointerfaces between the tiny unit cells after potassiation, ex situ TEM images were collected in the full potassiation/depotassiation state. In the low-magnification TEM image at 0.01 V (Fig. S24) and 3.00 V (Fig. S25), huge micron-sized particles were transformed into fine nanoparticles with a size range of 5–10 nm, confirming the high-entropy-induced nanocrystalline effect.

Figs. 6a–i show the HRTEM, fast Fourier transform (FFT), and inverse FFT (IFFT) images of various heterointerfaces. According to the valence change results obtained in Operando XAS, the possible potassiation products of each element in the HEMC@C included Ag, K_2Te, K_2Se, K_3Sb, and KSn [76]. The diffraction peaks of KSn and K_2Se could be observed in the FFT image, and the IFFT pattern corresponded to the (321) plane of KSn and the (311) plane of K_2Se. Fig. 6b shows the heterointerface image of K_3Sb and K_2Te. The diffraction peaks of K_3Sb and

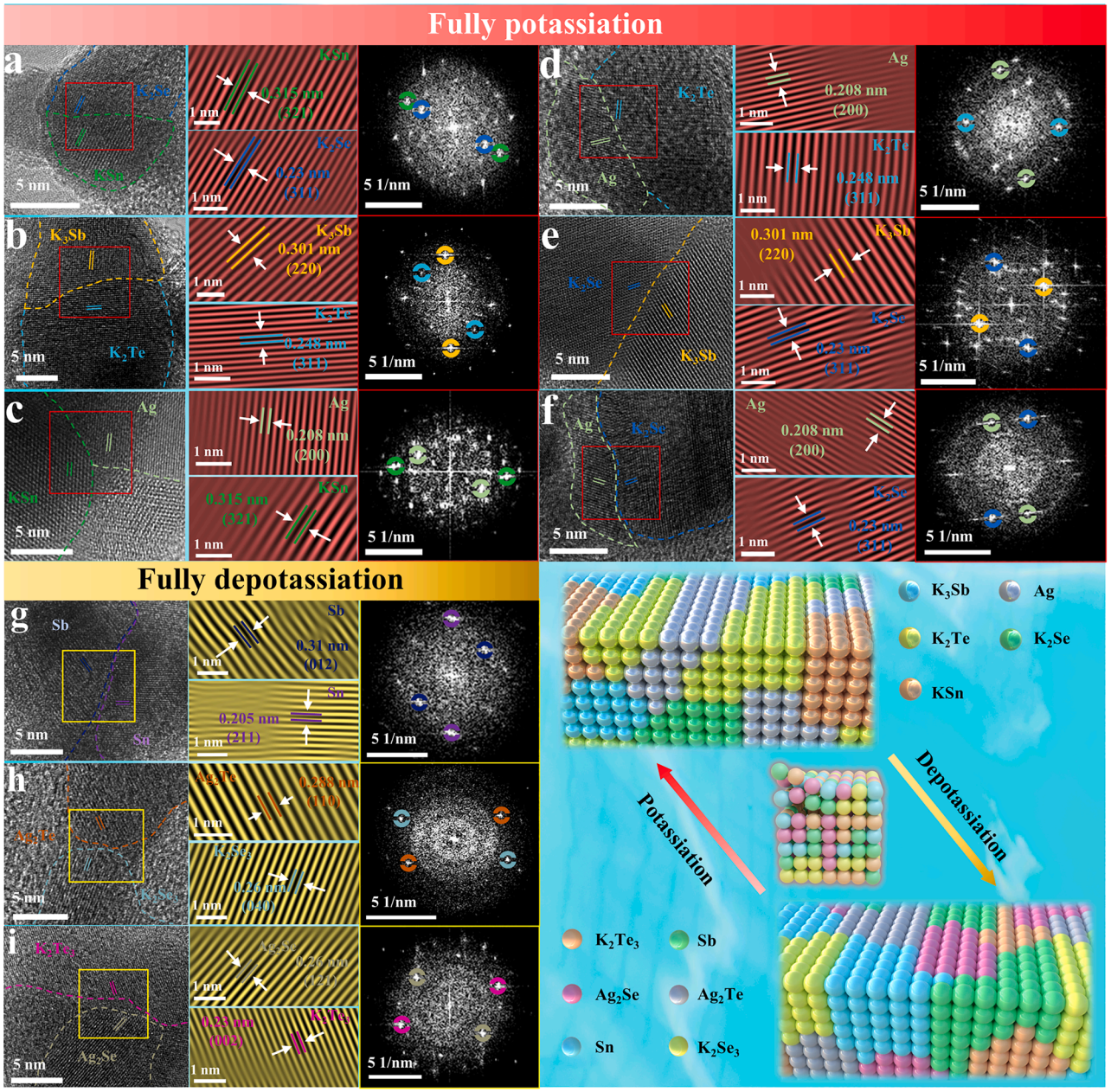

Fig. 6. Ex situ TEM analysis of HEME@C. HRTEM, FFT, and corresponding IFFT image of (a) KSn/K_2Se, (b) K_3Sb/K_2Te, (c) Ag/KSn, (d) Ag/K_2Te, (e) K_3Sb/KSn, (f) Ag/K_2Se, (g) Sn/Sb, (h) Ag_2Te/K_2Se_3 and (i) Ag_2Se/K_2Te_3 heterointerfaces. (j) Schematic illustration of the formation of short-range tiny cells and various heterointerfaces.

K_2Te could be observed in the FFT image, and the IFFT pattern corresponded to the (220) plane of K_3Sb and (311) plane of K_2Te. The Ag and KSn heterointerface is shown in Fig. 6c; the calculated D-spacings corresponded to Ag and KSn. Figs. 6e, f show the images of the heterojunction interfaces between Ag/K_2Te and Ag/K_2Se. The (200) plane of Ag, (311) plane of K_2Te, and (311) plane K_2Se with the corresponding D-spacing could be observed in the FFT and IFFT images. Fig. 6f shows the boundary, FFT, and the FFT images of the heterojunction interface between K_3Sb and K_2Te. During depotassiation, possible depotassiation products included Ag_2Se, Ag_2Te, Sn, Sb, K_2Se_3, and K_2Te_3, and the heterojunction interface between Sb and Sn with the corresponding FFT and IFFT images are shown in Fig. 6g. Furthermore, Fig. 6h shows the image of the heterojunction interface between Ag_2Te and K_2Se_3. In the FFT image, the diffraction points of Ag_2Te and K_2Se_3 could be observed, and the (110) plane of Ag_2Te and the (040) plane of K_2Se_3 were obtained from the IFFT image. Fig. 6i shows the image of the heterojunction interface between Ag_2Se and K_2Te_3. In the FFT image, the diffraction points of Ag_2Se and K_2Te_3 could be observed, which corresponded to the

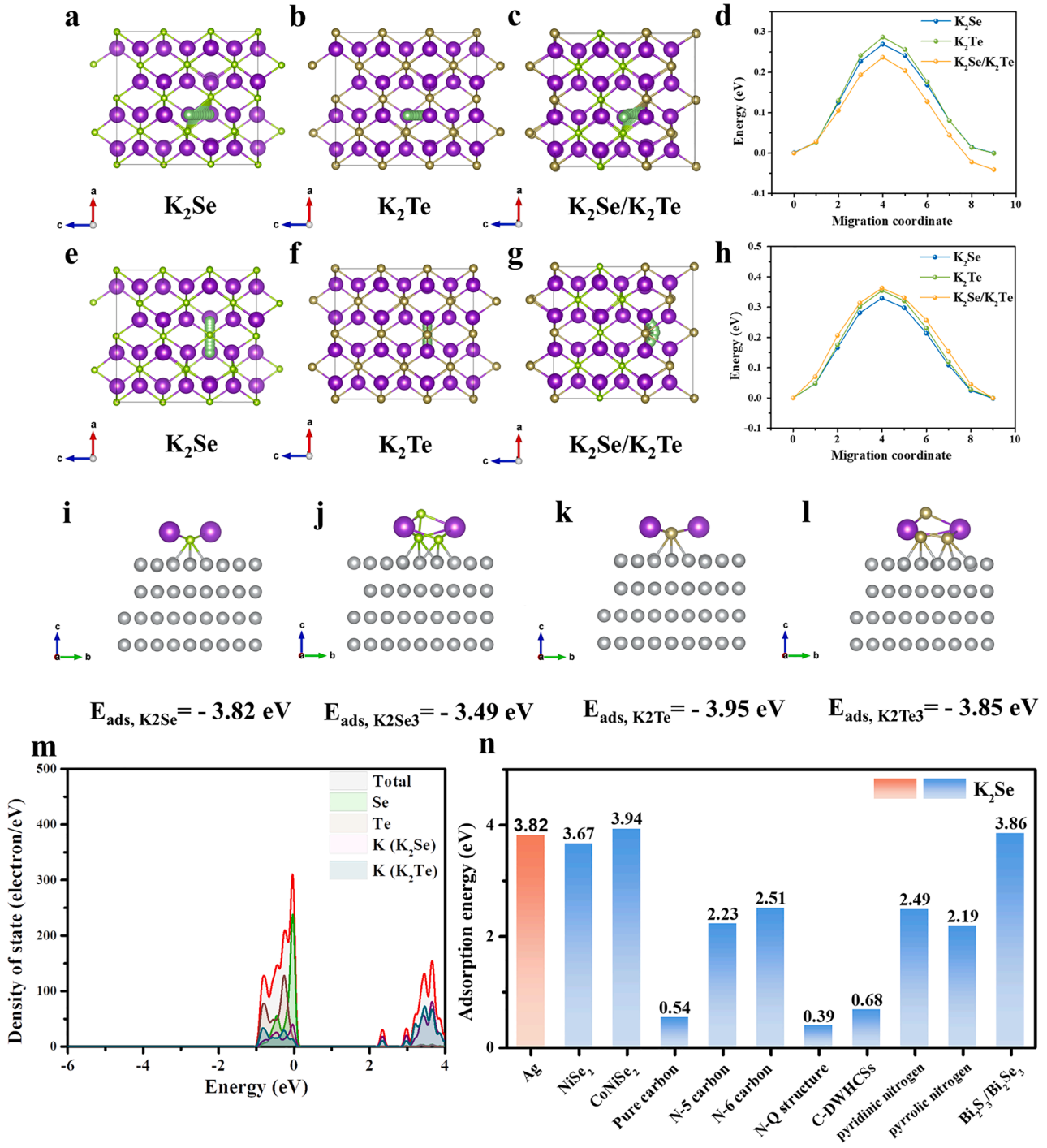

Fig. 7. Theoretical calculation of the diffusion barrier and adsorption energy. The diffusion path of K^+ along the horizontal direction between (a) K_2Se, (b) K_2Te, and (c) K_2Se/K_2Te heterointerfaces. (d) Diffusion barrier of K^+ along the horizontal direction. Diffusion path of K^+ along the vertical direction between (e) K_2Se, (f) K_2Te, and (g) K_2Se/K_2Te heterointerfaces. (h) Diffusion barrier of K^+ along the vertical direction. (m) Calculated DOS of the K_2Se/K_2Te heterointerface. (n) Comparison of K_2Se adsorption energy between Ag and other materials.

(110) plane of Ag_2Se and the (040) plane of K_2Te_3 in the IFFT pattern. Fig. 6j illustrates the process of the in situ formation of tiny cells with various heterointerfaces. The HEMC rock-salt structure could not withstand the volume expansion caused by the K^+ migration, resulting in the formation of many tiny cells. The synergistic effect of the increased heterostructures between these tiny cells provide rapid and stable K^+ storage through the built-in electric field. We selected the unique K_2Te and K_2Se heterostructures of the HEMC@C to calculate the diffusion barrier of K^+ using DFT to clarify why HEMC@C has a superior ion diffusion coefficient.

2.5. DFT calculation

The rate performance of PIB electrode materials is related to the mobility of K^+ in the lattice. Thus, the nudged elastic band (CI-NEB) method (see the experimental part for details) was used to calculate K^+ diffusion barriers in K_2Se, K_2Te, and K_2Se/K_2Te heterointerfaces to verify the influence of heterointerfaces on K^+ diffusion. First, the minimum energy paths of three materials were selected and plotted separately, as shown in Figs. 7a–c. According to the calculated results (Fig. 7d), the maximum K^+ diffusion barriers in K_2Se and K_2Te lattices were 0.27 and 0.29 eV, respectively. Meanwhile, the K_2Se/K_2Te heterointerface had a minimum diffusion barrier of 0.24 eV, which may be attributed to K_2Se. The ideal coupling of the interface with K_2Te produces a large number of charge interactions, thereby generating an internal electric field to promote the rapid diffusion of K^+ [77]. According to the Arrhenius equation [78],

$$D = D_0 \exp - QRT \tag{7}$$

where D_0 is a pre-exponential constant, Q is the activation energy, T is the absolute temperature, and R is the gas constant. Using Eq. (7), the diffusion energy barrier difference of 0.03 eV at room temperature promoted the K^+ diffusion rate 3.5 times, corresponding to the diffusion coefficient calculated using GITT, where HEMC@C has a higher diffusion coefficient. Next, the vertical diffusion paths of K^+ are plotted in Figs. 7e–g. Fig. 7h shows the diffusion energy barriers of K_2Se, K_2Te, and K_2Se/K_2Te heterointerfaces as 0.33, 0.35, and 0.36 eV, respectively, indicating that the diffusion K^+ in the heterointerface tends to be more horizontal. The PDOS cubic K_2Se/K_2Te heterointerfaces are shown in Fig. 7m. During heterointerface formation, the downshifting of the band gap to near Fermi levels compared with individual K_2Se and K_2Te (Fig. S26) connoted optimized electrical conductivity. Furthermore, in the presence of inert Ag, the adsorption energies of metallic Ag for potassium polyselenide and polytelluride are plotted in Figs. 7i–l. The interactions between metals and polyselenides and polytellurides followed the Lewis acid principle, and Se and Te atoms tended to bond with metals to form Ag–Se and Ag–Te bonds [79]. In the adsorption energy calculation, a vacuum height of 20 Å along the vertical direction was selected to avoid unwanted interactions between the slab and its period images. The adsorption energies of metal Ag with K_2Se, K_2Se_3, K_2Te, and K_2Te_3 were −3.82, −3.49, −3.95, and −3.85 eV, respectively, indicating good anchoring ability. The adsorption energies of potassium polyselenium and polytelluride were comparable with those considered to have strong adsorption ability (Fig. 7m) [60,80-83]. From these results, we deduce that the cocktail effect influences the synergistic effect for the conversion and alloy-type high-entropy materials, whether the metals are active or not.

2.6. Coin/pouch-type full-cell performance

A coin-type full cell with the HEMC@C as the anode and Prussian blue (PB) as the cathode was constructed to evaluate the feasibility of the HEMC@C. PB nanoparticles were prepared using the coprecipitation method. All the diffraction peaks in the XRD pattern (Fig. S27a) index were face-centered cubic $Fe_4[Fe(CN)_6]_3$ (JCPDS-52–1907). The electrochemical performance of the PB half cell is presented in Fig. S27b. A specific capacity of approximately 67 mAh g^{-1} was obtained at the current density of 100 mA g^{-1} with a working window of 2.00–4.00 V. Therefore, the working window of the HEMC@C||PB full cells was set to 1.00–3.80 V to ensure full utilization of the anode and avoid electrolyte decomposition. Fig. 8a presents the working principle of HEMC@C||PB full cells. PB as a cathode undergoes alloying reactions, whereas the HEMC@C anode undergoes alloying and conversion reactions. Fig. 8b shows the CV curves of the HEMC@C||PB full cells. Characteristic redox peaks of the HEMC@C and PB were observed; the curves highly overlapped, indicating good cycling performance. Fig. 8c shows a typical QV diagram of the HEMC@C||PB full cells and the corresponding half cell, and an obvious specific capacity difference was observed. Therefore, the mass ratio of the anode and cathode active materials was set to 1:6. Figs. 8d, e show the rate performance of the HEMC@C||PB full cells, exhibiting specific capacities of 364, 330, 299, 264, 199, and 141 mAh g^{-1} at current densities of 100, 200, 300, 500, 1000, and 2000 mA g^{-1}, respectively. Notably, when the current density was back to 100 mA g^{-1}, the specific capacity returned to 347 mAh g^{-1}, demonstrating satisfactory stability in high-rate conditions. Fig. 8f shows the energy density and corresponding power density at different current densities. The HEMC@C||PB full cells achieved a maximum energy density and power density of 200.4 Wh kg^{-1} and 8022.4 W kg^{-1}, respectively. HEMC@C||PB exhibited a specific capacity of 340 mAh g^{-1} after 250 cycles at a current density of 300 mA g^{-1} (Fig. 8g); the retention relative 10th cycle was 99%. A pouch-type battery was assembled to demonstrate whether it can be commercialized. Fig. 8h shows the structure of the pouch-type battery, where the cathode and anode were pre-potassiated before assembly. As shown in Fig. 8i, the HEMC@C||PB pouch-type battery can easily light up many light-emitting diodes (LEDs), and the GCD curves and cycling stability are shown in Fig. S28, demonstrating its considerable application prospects in energy storage devices.

3. Conclusion

The NaCl-type rock-salt-structure material prepared using a one-step melting method had adjustable anion and cation sites. The mixing temperature, redox compatibility, bond softness, and geometric optimization were considered to elucidate the possibility of cations in the rock-salt structure. We confirmed that the NaCl-type rock-salt structure introduced by high-entropy engineering can significantly improve the K^+ storage ability and cycling stability with the increase in entropy. Moreover, the reaction mechanism of HEMC@C was proposed to further analyze the relationship between entropy and electrochemical performance. The significantly improved HEMC@C performance was due to the in-situ-formed tiny unit cells and various heterogeneous interfaces during the phase-change energy storage reaction, resulting in the redistribution of electrons, which promoted charge transfer and ion diffusion. The results of the kinetic analysis and theoretical calculations support the following conclusions: (i) the heterointerface between the potassiation products can effectively reduce the diffusion barrier of K^+ and (ii) inactive metal silver provides excellent adsorption energy for polyselenides and polytellurides. The rational design of active and inactive metals and entropy configurations can enhance the reversible cycling ability of conversion and alloy reactions. This work provides a new strategy for designing and developing secondary battery anode materials considering entropy configuration and element coordination.

CRediT authorship contribution statement

Che-Bin Chang: Conceptualization, Methodology, Data curation. **Ying-Rui Lu:** Data curation. **Hsing-Yu Tuan:** Conceptualization, Resources, Supervision, Writing – review & editing.

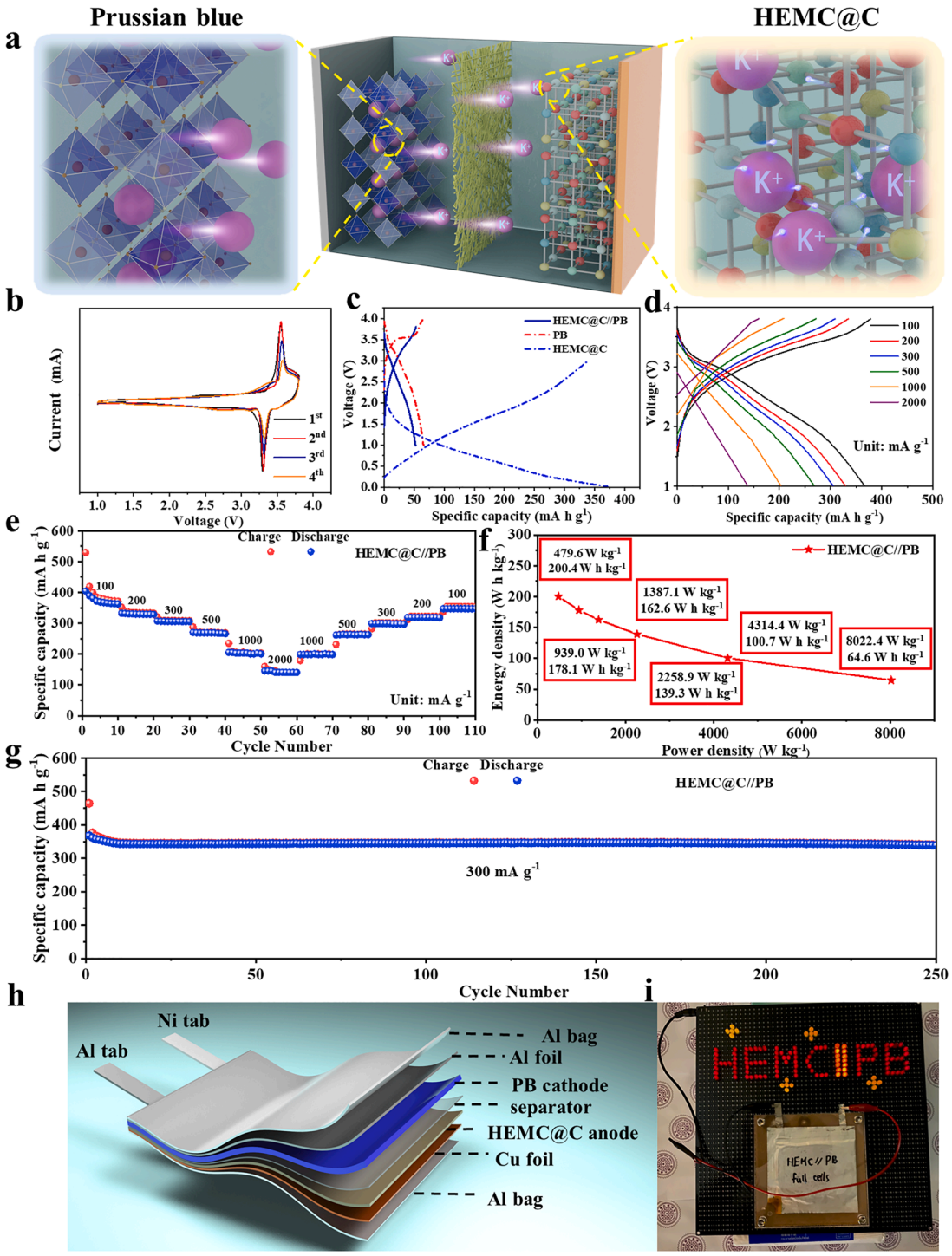

Fig. 8. Electrochemical performance of HEMC@C//PB full cells. (a) Schematic working principle of HEMC@C//PB full cells. (b) CV curves of HEMC@C//PB full cells. (c) QV curves of HEMC@C, PB, and HEMC@C//PB full cells. (d) QV curves of HEMC@C//PB full cells at different current densities. (e) Rate capability of HEMC@C//PB full cells. (f) Ragone plots of HEMC@C//PB full cells. (g) Long-term cycling performance of HEMC@C//PB full cells. (h) Schematic illustration of the pouch-type HEMC@C//PB full cells. (i) Photograph of LEDs lightened by the pouch-type HEMC@C//PB full cells.

Declaration of Competing Interest

The authors declare no competing financial interest.

Acknowledgment

This work was supported by the financial support from the 2030 Cross-Generation Young Scholars Program by Ministry of Science and Technology, Taiwan (MOST 111-2628-E-007 -008). H.-Y. Tuan also acknowledges the financial support of National Tsing Hua University, Taiwan, through the grant of 111QI030E1. The authors thank the technical support from Ms. Y. M. Chang in Instrumentation Center at National Tsing Hua University.

Supplementary materials

Supplementary material associated with this article can be found, in the online version, at doi:10.1016/j.ensm.2023.102770.

References

[1] T.M. Gür, Review of electrical energy storage technologies, materials and systems: challenges and prospects for large-scale grid storage, Energy Environ. Sci. 11 (2018) 2696–2767, https://doi.org/10.1039/C8EE01419A.

[2] A. Poullikkas, A comparative overview of large-scale battery systems for electricity storage, Renew. Sustain. Energy Rev. 27 (2013) 778–788, https://doi.org/10.1016/j.rser.2013.07.017.

[3] S. Hameer, J.L. van Niekerk, A review of large-scale electrical energy storage, Int. J. Energy Res. 39 (2015) 1179–1195, https://doi.org/10.1002/er.3294.

[4] C. Choi, D.S. Ashby, D.M. Butts, R.H. DeBlock, Q. Wei, J. Lau, B. Dunn, Achieving high energy density and high power density with pseudocapacitive materials, Nat. Rev. Mater. 5 (2020) 5–19, https://doi.org/10.1038/s41578-019-0142-z.

[5] J.W. Choi, D. Aurbach, Promise and reality of post-lithium-ion batteries with high energy densities, Nat. Rev. Mater. 1 (2016) 1–16, https://doi.org/10.1038/natrevmats.2016.13.

[6] S. Ji, Y. Zheng, K.S. Hui, J. Li, K. Wang, C. Song, H. Xu, S. Wang, C. Zha, D.A. Dinh, Z. Tang, Z. Shao, KN, Enhanced electrochemical and environmental stability of black phosphorus-derived phosphorus composite anode for safe potassium-ion battery using amorphous zinc phosphate as a multi-functional additive, Energy Storage Materials 57 (2023), https://doi.org/10.1016/j.ensm.2023.01.036.

[7] T.C. Wanger, The Lithium future—Resources, recycling, and the environment, Conserv. Lett. 4 (2011) 202–206, https://doi.org/10.1111/j.1755-263X.2011.00166.x.

[8] C. Zhang, H. Zhao, Y. Lei, Recent research progress of anode materials for potassium-ion batteries, Energy Environ. Mater. 3 (2020) 105–120, https://doi.org/10.1002/eem2.12059.

[9] A. Eftekhari, Z. Jian, X. Ji, Potassium secondary batteries, ACS Appl. Mater. Interfaces 9 (2017) 4404–4419, https://doi.org/10.1021/acsami.6b07989.

[10] L. Fan, Y. Hu, A.M. Rao, J. Zhou, Z. Hou, C. Wang, B. Lu, Prospects of electrode materials and electrolytes for practical potassium-based batteries, Small Methods 5 (2021), 2101131, https://doi.org/10.1002/smtd.202101131.

[11] S. Liu, L. Kang, S.C. Jun, Challenges and strategies toward cathode materials for rechargeable potassium-ion batteries, Adv. Mater. 33 (2021), 2004689, https://doi.org/10.1002/adma.202004689.

[12] X. Min, J. Xiao, M. Fang, W.A. Wang, Y. Zhao, Y. Liu, A.M. Abdelkader, K. Xi, R. V. Kumar, Z. Huang, Potassium-ion batteries: outlook on present and future technologies, Energy Environ. Sci. 14 (2021) 2186–2243, https://doi.org/10.1039/D0EE02917C.

[13] R. Rajagopalan, Y. Tang, X. Ji, C. Jia, H. Wang, Advancements and challenges in potassium ion batteries: a comprehensive review, Adv. Funct. Mater. 30 (2020), 1909486, https://doi.org/10.1002/adfm.201909486.

[14] L. Fan, R. Ma, Q. Zhang, X. Jia, B. Lu, Graphite anode for a potassium-ion battery with unprecedented performance, Angew. Chem. 131 (2019) 10610–10615, https://doi.org/10.1002/ange.201904258.

[15] Y. Lei, D. Han, J. Dong, L. Qin, X. Li, D. Zhai, B. Li, Y. Wu, F. Kang, Unveiling the influence of electrode/electrolyte interface on the capacity fading for typical graphite-based potassium-ion batteries, Energy Storage Mater. 24 (2020) 319–328, https://doi.org/10.1016/j.ensm.2019.07.043.

[16] X. Wang, Z. Luo, J. Huang, Z. Chen, T. Xiang, Z. Feng, J. Wang, S. Wang, Y. Ma, H. Yang, S/N-co-doped graphite nanosheets exfoliated via three-roll milling for high-performance sodium/potassium ion batteries, J. Mater. Sci. Technol. 147 (2023) 47–55, https://doi.org/10.1016/j.jmst.2022.11.015.

[17] K. Song, C. Liu, L. Mi, S. Chou, W. Chen, C. Shen, Recent Progress on the Alloy-Based Anode for Sodium-Ion Batteries and Potassium-Ion Batteries, Small 17 (2021), 1903194, https://doi.org/10.1002/smll.201903194.

[18] B. Babu, C. Neumann, S. Muench, M. Enke, L. Medenbach, C. Leibing, A. Lex-Balducci, A. Turchanin, U.S. Schubert, A. Balducci, Diglyme-based gel polymer electrolytes for K-ion capacitors, Energy Storage Mater. 56 (2023) 342–350, https://doi.org/10.1016/j.ensm.2023.01.031.

[19] S. Chong, L. Yuan, T. Li, C. Shu, S. Qiao, S. Dong, Z. Liu, J. Yang, H.K. Liu, S.X. Dou, Nitrogen and oxygen co-doped porous hard carbon nanospheres with core-shell architecture as anode materials for superior potassium-ion storage, Small 18 (2022), 2104296, https://doi.org/10.1002/smll.202104296.

[20] X. Zhang, H. Zhu, Q. He, T. Xiong, X. Wang, Z. Xiao, H. Wang, Y. Zhao, L. Xu, L. Mai, K+ induced phase transformation of layered titanium disulfide boosts ultrafast potassium-ion storage, Adv. Funct. Mater. 32 (2022), 2205330, https://doi.org/10.1002/adfm.202205330.

[21] Y. Du, Z. Yi, Z. Zhang, J. Liao, Y. Xu, J. Bao, X. Zhou, A highly stable potassium-ion battery anode enabled by multilayer graphene sheets embedded with SnTe nanoparticles, Chem. Eng. J. 435 (2022), 135100, https://doi.org/10.1016/j.cej.2022.135100.

[22] J. He, Y. Wei, T. Zhai, H. Li, Antimony-based materials as promising anodes for rechargeable lithium-ion and sodium-ion batteries, Mater. Chem. Front. 2 (2018) 437–455, https://doi.org/10.1039/C7QM00480J.

[23] Y.-.H. Zhu, Q. Zhang, X. Yang, E.-.Y. Zhao, T. Sun, X.-.B. Zhang, S. Wang, X.-.Q. Yu, J.-.M. Yan, Q. Jiang, Reconstructed orthorhombic V_2O_5 polyhedra for fast ion diffusion in K-ion batteries, Chem. 5 (2019) 168–179, https://doi.org/10.1016/j.chempr.2018.10.004.

[24] H. Tan, Y. Feng, X. Rui, Y. Yu, S. Huang, Metal chalcogenides: paving the way for high-performance sodium/potassium-ion batteries, Small Methods 4 (2020), 1900563, https://doi.org/10.1002/smtd.201900563.

[25] B. Chen, J. Ding, X. Bai, H. Zhang, M. Liang, S. Zhu, C. Shi, L. Ma, E. Liu, N. Zhao, Engineering pocket-like graphene–shell encapsulated FeS_2: inhibiting polysulfides shuttle effect in potassium-ion batteries, Adv. Funct. Mater. 32 (2022), 2109899, https://doi.org/10.1002/adfm.202109899.

[26] Y. Wu, Z. Wang, Z. Wang, X. Liu, S. Zhang, C. Deng, Tailoring stress-relieved structure for ternary cobalt phosphoselenide@ N/P codoped carbon towards high-performance potassium-ion hybrid capacitors and potassium-ion batteries, Energy Storage Mater. 57 (2023) 180–194, https://doi.org/10.1016/j.ensm.2023.02.013.

[27] H. Tian, H. Tian, S. Wang, S. Chen, F. Zhang, L. Song, H. Liu, J. Liu, G. Wang, High-power lithium–selenium batteries enabled by atomic cobalt electrocatalyst in hollow carbon cathode, Nat. Commun. 11 (2020) 1–12, https://doi.org/10.1038/s41467-020-18820-y.

[28] T. Yim, M.-.S. Park, J.-.S. Yu, K.J. Kim, K.Y. Im, J.-.H. Kim, G. Jeong, Y.N. Jo, S.-.G. Woo, K.S. Kang, Effect of chemical reactivity of polysulfide toward carbonate-based electrolyte on the electrochemical performance of Li–S batteries, Electrochim. Acta 107 (2013) 454–460, https://doi.org/10.1016/j.electacta.2013.06.039.

[29] J.S. Lee, J.-.S. Park, K.W. Baek, R. Saroha, S.H. Yang, Y.C. Kang, J.S. Cho, Coral-like porous microspheres comprising polydopamine-derived N-doped C-coated $MoSe_2$ nanosheets composited with graphitic carbon as anodes for high-rate sodium-and potassium-ion batteries, Chem. Eng. J. 456 (2023), 141118, https://doi.org/10.1016/j.cej.2022.141118.

[30] J. Zhang, G. Kim, M. Park, J. Zhang, S. Lee, Y. Cui, K. Zhang, F. Zou, Y.M. Kang, Nanostructuring-promoted non-equilibrium phase transformation of Bi anodes toward diffusion-controlled reaction for K-ion batteries, Adv. Energy Mater. 12 (2022), 2202446, https://doi.org/10.1002/aenm.202202446.

[31] Y.-.Y. Hsieh, K.-.T. Chen, H.-.Y. Tuan, A synergetic SnSb-amorphous carbon composites prepared from polyesterification process as an ultrastable potassium-ion battery anode, Chem. Eng. J. 420 (2021), 130451, https://doi.org/10.1016/j.cej.2021.130451.

[32] X. Ge, S. Liu, M. Qiao, Y. Du, Y. Li, J. Bao, X. Zhou, Enabling superior electrochemical properties for highly efficient potassium storage by impregnating ultrafine Sb nanocrystals within nanochannel-containing carbon nanofibers, Angew. Chem. Int. Ed. 58 (2019) 14578–14583, https://doi.org/10.1002/anie.201908918.

[33] J. Tang, C.-.Y. Wang, F. Xiu, A.J. Hong, S. Chen, M. Wang, C. Zeng, H.-.J. Yang, H.-.Y. Tuan, C.-.J. Tsai, Single-crystalline $Ni_2Ge/Ge/Ni_2Ge$ nanowire heterostructure transistors, Nanotechnology 21 (2010), 505704. https://10.1088/0957-4484/21/50/505704.

[34] B. Zhang, B. Xu, Z. Xiao, L. Cao, H. Geng, X. Ou, Inner-stress-dissipative, rapid self-healing core-shell sulfide quantum dots for remarkable potassium-ion storage, Energy Storage Mater. 56 (2023) 96–107, https://doi.org/10.1016/j.ensm.2023.01.007.

[35] L. Cao, B. Zhang, H. Xia, C. Wang, B. Luo, X. Fan, J. Zhang, X. Ou, Hierarchical chrysanthemum-like MoS_2/Sb heterostructure encapsulated into N-doped graphene framework for superior potassium-ion storage, Chem. Eng. J. 387 (2020), 124060, https://doi.org/10.1016/j.cej.2020.124060.

[36] C. Wei, L. Tan, Y. Zhang, B. Xi, S. Xiong, J. Feng, MXene/organics heterostructures enable ultrastable and high-rate lithium/sodium batteries, ACS Appl. Mater. Interfaces 14 (2022) 2979–2988, https://doi.org/10.1021/acsami.1c22787.

[37] P. Xiong, J. Wu, M. Zhou, Y. Xu, Bismuth–antimony alloy nanoparticle@ porous carbon nanosheet composite anode for high-performance potassium-ion batteries, ACS Nano 14 (2019) 1018–1026, https://doi.org/10.1021/acsnano.9b08526.

[38] A. Amiri, R. Shahbazian-Yassar, Recent progress of high-entropy materials for energy storage and conversion, J. Mater. Chem. A 9 (2021) 782–823, https://doi.org/10.1039/D0TA09578H.

[39] C.M. Rost, E. Sachet, T. Borman, A. Moballegh, E.C. Dickey, D. Hou, J.L. Jones, S. Curtarolo, J.-.P. Maria, Entropy-stabilized oxides, Nat. Commun. 6 (2015) 1–8, https://doi.org/10.1038/ncomms9485.

[40] X. Mao, Q. Chen, S. Granick, Entropy favours open colloidal lattices, Nat. Mater. 12 (2013) 217–222, https://doi.org/10.1038/nmat3496.

[41] S.-.C. Lu, M.-.C. Hsiao, M. Yorulmaz, L.-.Y. Wang, P.-.Y. Yang, S. Link, W.-.S. Chang, H.-.Y. Tuan, Single-crystalline copper nano-octahedra, Chem. Mater. 27 (2015) 8185–8188, https://doi.org/10.1021/acs.chemmater.5b03519.

[42] A. Sarkar, L. Velasco, D. Wang, Q. Wang, G. Talasila, L. de Biasi, C. Kübel, T. Brezesinski, S.S. Bhattacharya, H. Hahn, High entropy oxides for reversible energy storage, Nat. Commun. 9 (2018) 1–9, https://doi.org/10.1038/s41467-018-05774-5.

[43] J. Zhao, Y. Zhang, X. Chen, G. Sun, X. Yang, Y. Zeng, R. Tian, F. Du, Entropy-change driven highly reversible sodium storage for conversion-type sulfide, Adv. Funct. Mater. 32 (2022), 2206531, https://doi.org/10.1002/adfm.202206531.

[44] D. Qiu, B. Zhang, T. Zhang, T. Shen, Z. Zhao, Y. Hou, Sulfur-doped carbon for potassium-ion battery anode: insight into the doping and potassium storage mechanism of sulfur, ACS Nano. 16 (2022) 21443–21451, https://doi.org/10.1021/acsnano.2c09845.

[45] Y. Luo, S. Hao, S. Cai, T.J. Slade, Z.Z. Luo, V.P. Dravid, C. Wolverton, Q. Yan, M. G. Kanatzidis, High thermoelectric performance in the new cubic semiconductor $AgSnSbSe_3$ by high-entropy engineering, J. Am. Chem. Soc. 142 (2020) 15187–15198, https://doi.org/10.1021/jacs.0c07803.

[46] B.S. Murty, J.-.W. Yeh, S. Ranganathan, P. Bhattacharjee, High-Entropy Alloys, Elsevier, 2019.

[47] Y. Zhang, Y. J. Zhou in solid solution formation criteria for high entropy alloys, Materials Science Forum, Trans Tech Publ: 2007; pp 1337–1339. 10.4028/www.scientific.net/MSF.561-565.1337.

[48] G. Hautier, C. Fischer, V. Ehrlacher, A. Jain, G. Ceder, Data mined ionic substitutions for the discovery of new compounds, Inorg. Chem. 50 (2011) 656–663, https://doi.org/10.1021/ic102031h.

[49] B. Vargas, E. Coutiño-Gonzalez, O. Ovalle-Encinia, C. Sánchez-Aké, D. Solis-Ibarra, Efficient emission in halide layered double perovskites: the role of Sb^{3+} substitution in $Cs_4Cd_{1-x}Mn_x Bi_2Cl_{12}$ phosphors, J. Phys. Chem. Lett. 11 (2020) 10362–10367, https://doi.org/10.1021/acs.jpclett.0c02912.

[50] Z. Lun, B. Ouyang, D.-.H. Kwon, Y. Ha, E.E. Foley, T.-.Y. Huang, Z. Cai, H. Kim, M. Balasubramanian, Y. Sun, Cation-disordered rocksalt-type high-entropy cathodes for Li-ion batteries, Nat. Mater. 20 (2021) 214–221, https://doi.org/10.1038/s41563-020-00816-0.

[51] F.-.W. Yuan, H.-.J. Yang, H.-.Y. Tuan, Seeded silicon nanowire growth catalyzed by commercially available bulk metals: broad selection of metal catalysts, superior field emission performance, and versatile nanowire/metal architectures, J. Mater. Chem. 21 (2011) 13793–13800, https://doi.org/10.1039/C1JM11956G.

[52] U. Mizutani, The Hume-Rothery rules for structurally complex alloy phases. Surface Properties and Engineering of Complex Intermetallics, World Scientific, 2010, pp. 323–399, https://doi.org/10.1142/9789814304771_0011.

[53] R.-.Z. Zhang, F. Gucci, H. Zhu, K. Chen, M.J. Reece, Data-driven design of ecofriendly thermoelectric high-entropy sulfides, Inorg. Chem. 57 (2018) 13027–13033, https://doi.org/10.1021/acs.inorgchem.8b02379.

[54] I. Brown, The bond-valence method: an empirical approach to chemical structure and bonding, Struct. Bond. Cryst. 2 (1981) 1–30.

[55] W. Wang, Y. Geng, Y. Qian, M. Ji, Y. Xie, A novel room temperature method to nanocrystalline Ag_2Se, Mater. Res. Bull. 34 (1999) 877–882, https://doi.org/10.1016/S0025-5408(99)00083-5.

[56] N.D. Boscher, C.J. Carmalt, R.G. Palgrave, I.P. Parkin, Atmospheric pressure chemical vapour deposition of SnSe and $SnSe_2$ thin films on glass, Thin Solid Films 516 (2008) 4750–4757, https://doi.org/10.1016/j.tsf.2007.08.100.

[57] J. Kaufman, S. Metin, D. Saperstein, Symmetry breaking in nitrogen-doped amorphous carbon: infrared observation of the Raman-active G and D bands, Phys. Rev. B 39 (1989) 13053, https://doi.org/10.1103/PhysRevB.39.13053.

[58] R. Bardestani, G.S. Patience, S. Kaliaguine, Experimental methods in chemical engineering: specific surface area and pore size distribution measurements—BET, BJH, and DFT, Can. J. Chem. Eng. 97 (2019) 2781–2791, https://doi.org/10.1002/cjce.23632.

[59] H. Wang, D. Zhai, F. Kang, Solid electrolyte interphase (SEI) in potassium ion batteries, Energy Environ. Sci. 13 (2020) 4583–4608, https://doi.org/10.1039/D0EE01638A.

[60] Y.-.Y. Hsieh, H.-.Y. Tuan, Architectural van der Waals Bi_2S_3/Bi_2Se_3 topological heterostructure as a superior potassium-ion storage material, Energy Storage Mater. 51 (2022) 789–805, https://doi.org/10.1016/j.ensm.2022.07.020.

[61] H. He, D. Sun, Y. Tang, H. Wang, M. Shao, Understanding and improving the initial Coulombic efficiency of high-capacity anode materials for practical sodium ion batteries, Energy Storage Mater. 23 (2019) 233–251, https://doi.org/10.1016/j.ensm.2019.05.008.

[62] C.-.H. Chang, K.-.T. Chen, Y.-.Y. Hsieh, C.-.B. Chang, H.-.Y. Tuan, Crystal facet and architecture engineering of metal oxide nanonetwork anodes for high-performance potassium ion batteries and hybrid capacitors, ACS Nano. 16 (2022) 1486–1501, https://doi.org/10.1021/acsnano.1c09863.

[63] B. Lee, M. Kim, S. Kim, J. Nanda, S.J. Kwon, H.D. Jang, D. Mitlin, S.W. Lee, High capacity adsorption—dominated potassium and sodium ion storage in activated crumpled graphene, Adv. Energy Mater. 10 (2020), 1903280, https://doi.org/10.1002/aenm.201903280.

[64] J. Ding, W. Hu, E. Paek, D. Mitlin, Review of hybrid ion capacitors: from aqueous to lithium to sodium, Chem. Rev. 118 (2018) 6457–6498, https://doi.org/10.1021/acs.chemrev.8b00116.

[65] T.C. Liu, W. Pell, B. Conway, S. Roberson, Behavior of molybdenum nitrides as materials for electrochemical capacitors: comparison with ruthenium oxide, J. Electrochem. Soc. 145 (1998) 1882. https://10.1149/1.1838571.

[66] X. Ren, D. Yu, L. Yuan, Y. Bai, K. Huang, J. Liu, S. Feng, In situ exsolution of Ag from $AgBiS_2$ nanocrystal anode boosting high-performance potassium-ion batteries, J. Mater. Chem. A 8 (2020) 15058–15065, https://doi.org/10.1039/D0TA03964K.

[67] H. Kim, G.O. Park, Y. Kim, S. Muhammad, J. Yoo, M. Balasubramanian, Y.-.H. Cho, M.-.G. Kim, B. Lee, K. Kang, New insight into the reaction mechanism for exceptional capacity of ordered mesoporous SnO_2 electrodes via synchrotron-based X-ray analysis, Chem. Mater. 26 (2014) 6361–6370, https://doi.org/10.1021/cm5025603.

[68] J. Tian, G. Han, H. Wei, Q. Zheng, T. Jin, X. Sun, Z. Hu, Effects of alloying elements on the electronic structure and ductility of NiAl compounds investigated by X-ray absorption fine structure, Philos. Mag. 93 (2013) 2161–2171, https://doi.org/10.1080/14786435.2013.765984.

[69] M. Bär, B.-.A. Schubert, B. Marsen, S. Schorr, R. Wilks, L. Weinhardt, S. Pookpanratana, M. Blum, S. Krause, Y. Zhang, Electronic structure of Cu_2ZnSnS_4 probed by soft x-ray emission and absorption spectroscopy, Phys. Rev. B 84 (2011), 035308, https://doi.org/10.1103/PhysRevB.84.035308.

[70] Y. Liu, Z. Tai, Q. Zhang, H. Wang, W.K. Pang, H.K. Liu, K. Konstantinov, Z. Guo, A new energy storage system: rechargeable potassium-selenium battery, Nano Energy 35 (2017) 36–43. 10.1016/j.nanoen.2017.03.029.

[71] C.-.Y. Tsai, C.-.H. Chang, T.-.L. Kao, K.-.T. Chen, H.-.Y. Tuan, Shape matters: $SnP_{0.94}$ teardrop nanorods with boosted performance for potassium ion storage, Chem. Eng. J. 417 (2021), 128552, https://doi.org/10.1016/j.cej.2021.128552.

[72] S. Chong, S. Qiao, X. Wei, T. Li, L. Yuan, S. Dong, W. Huang, Sb2S3-based conversion-alloying dual mechanism anode for potassium-ion batteries, iScience 24 (2021) 103494. 10.1016/j.isci.2021.103494.

[73] J. Cao, L. Wang, D. Li, Z. Yuan, H. Xu, J. Li, R. Chen, V. Shulga, G. Shen, W. Han, $Ti_3C_2T_x$ MXene conductive layers supported bio-derived $Fe_{x-1}Se_x$/MXene/carbonaceous nanoribbons for high-performance half/full sodium-ion and potassium-ion batteries, Adv. Mater. 33 (2021), 2101535, https://doi.org/10.1002/adma.202101535.

[74] S. Dong, D. Yu, J. Yang, L. Jiang, J. Wang, L. Cheng, Y. Zhou, H. Yue, H. Wang, L. Guo, Tellurium: a high-volumetric-capacity potassium-ion battery electrode material, Adv. Mater. 32 (2020), 1908027, https://doi.org/10.1002/adma.201908027.

[75] A.A. Bunaciu, E.G. UdriŞTioiu, H.Y. Aboul-Enein, X-ray diffraction: instrumentation and applications, Crit. Rev. Anal. Chem. 45 (2015) 289–299, https://doi.org/10.1080/10408347.2014.949616.

[76] K.-.T. Chen, S. Chong, L. Yuan, Y.-.C. Yang, H.-.Y. Tuan, Conversion-alloying dual mechanism anode: nitrogen-doped carbon-coated Bi_2Se_3 wrapped with graphene for superior potassium-ion storage, Energy Storage Mater. 39 (2021) 239–249, https://doi.org/10.1016/j.ensm.2021.04.019.

[77] N. Zhao, J. Qin, L. Chu, L. Wang, D. Xu, X. Wang, H. Yang, J. Zhang, X. Li, Heterogeneous interface of Se@ Sb@ C boosting potassium storage, Nano Energy 78 (2020), 105345, https://doi.org/10.1016/j.nanoen.2020.105345.

[78] Y. Du, Y. Chang, B. Huang, W. Gong, Z. Jin, H. Xu, Z. Yuan, Y. Liu, Y. He, F.-.Y. Xie, Diffusion coefficients of some solutes in fcc and liquid Al: critical evaluation and correlation, Mater. Sci. Eng. A 363 (2003) 140–151, https://doi.org/10.1016/S0921-5093(03)00624-5.

[79] F. Zhang, X. Guo, P. Xiong, J. Zhang, J. Song, K. Yan, X. Gao, H. Liu, G. Wang, Interface engineering of MXene composite separator for high-performance Li–Se and Na–Se batteries, Adv. Energy Mater. 10 (2020), 2000446, https://doi.org/10.1002/aenm.202000446.

[80] X. Wu, X. Chen, H. Wu, B. Xie, D. Wang, R. Wang, X. Zhang, Y. Piao, G. Diao, M. Chen, Encapsulation of Se in dual-wall hollow carbon spheres: physical confinement and chemisorption for superior Na–Se and K–Se batteries, Carbon 187 (2022) 354–364, https://doi.org/10.1016/j.carbon.2021.11.013.

[81] H. Liu, Q. Wang, X. Sun, H. Gou, C. Zhang, G. Wang, Carbon host pore structure regulation boosting fast and stable Se-K electrochemistry towards Se-K ion capacitors, Carbon 203 (2022) 141–151, https://doi.org/10.1016/j.carbon.2022.11.044.

[82] Y. Ding, J. Cai, Y. Sun, Z. Shi, Y. Yi, B. Liu, J. Sun, Bimetallic selenide decorated nanoreactor synergizing confinement and electrocatalysis of Se species for 3D-printed high-loading K–Se batteries, ACS Nano 16 (2022) 3373–3382, https://doi.org/10.1021/acsnano.2c00256.

[83] Y. Yao, R. Xu, M. Chen, X. Cheng, S. Zeng, D. Li, X. Zhou, X. Wu, Y. Yu, Encapsulation of SeS_2 into nitrogen-doped free-standing carbon nanofiber film enabling long cycle life and high energy density K-SeS_2 battery, ACS Nano 13 (2019) 4695–4704, https://doi.org/10.1021/acsnano.9b00980.